# Energetics of the complex phase diagram of a tunable bilayer graphene probed by quantum capacitance

Manabendra Kuiri and Anindya Das*
*Department of Physics, Indian Institute of Science, Bangalore 560012, India*

(Received 22 October 2018; revised manuscript received 21 December 2018; published 11 March 2019)

Bilayer graphene provides a unique platform to explore the rich physics in quantum Hall effect. The unusual combination of spin, valley, and orbital degeneracy leads to interesting symmetry-broken states with electric and magnetic field. Conventional transport measurements, like resistance measurements, have been performed to probe the different ordered states in bilayer graphene. However, not much work has been done to directly map the energetics of those states in bilayer graphene. Here, we have carried out the magnetocapacitance measurements with electric and magnetic field in a hexagonal boron nitride encapsulated dual-gated bilayer graphene device. At zero magnetic field, using the quantum capacitance technique we measure the gap around the charge neutrality point as a function of perpendicular electric field and the obtained value of the gap matches well with the theory. In the presence of a perpendicular magnetic field, we observe Landau-level crossing in our magnetocapacitance measurements with electric field. The gap closing and reopening of the lowest Landau level with electric and magnetic field shows the transition from one ordered state to another. Furthermore, we observe the collapsing of the Landau levels near the band edge at higher electric field ($\bar{D} > 0.5$ V/nm), which was predicted theoretically. The complete energetics of the Landau levels of bilayer graphene with electric and magnetic field in our experiment paves the way to unravel the nature of ground states of the system.

DOI: 10.1103/PhysRevB.99.125411

## I. INTRODUCTION

Bilayer graphene (BLG) provides a unique two-dimensional system in condensed matter physics, where the low energy spectrum is gapless touching at $K$ and $K'$ points and an external electric field opens up a tunable gap at the valley points [1,2]. In clean samples the $e-e$ interactions lead to gap opening even without an external electric field [3,4], and interesting phases, such as quantum-spin-Hall, anomalous quantum Hall [5], layer antiferromagnet [6], and nematic [7] states, were suggested to be the possible ground state at the neutrality point [8]. Bilayer graphene is even more interesting in the presence of magnetic field due to the additional orbital degeneracy of the lowest Landau level (LL) together with spin and valley degeneracy, resulting in complex quantum Hall states (QHS) [9,10]. The coupling of electric and magnetic fields leads to transitions between different spin, valley, and orbital ordering, leading to unique interaction-driven symmetry-broken states [11–21]. Thus BLG provides an excellent platform to probe the phase transitions between different ordered states [22–25].

There have been extensive studies to find the nature of ordered states in BLG, both theoretically [24–26] and experimentally [13,16,20,27,28]. The model employed in Refs. [16,23,25] shows that at finite magnetic field ($B$), the LLs are spin split and the orbital and valley degeneracies are lifted by the application of electric field. However, the model employed in Refs. [13,28] showed that at finite $B$ both the spin and orbital degeneracies are lifted and the application of electric field results in lifting the valley degeneracy only. However, there is no common consensus about the order of the ground state of these symmetry-broken states [13–15].

Recent transport measurements in a dual-gated geometry have observed the crossing of LLs leading to the closing of gap which is attributed to the phase transition between different types of ordered states [20,27]. Although transport measurements can provide an indication of gap size, the true energetics of these states cannot be estimated by conventional transport measurements. Therefore, thermodynamic measurement is desirable to directly probe the electronic properties as well as the energetics of these states [29]. The proper knowledge of the energetics of these LL crossing points, together with the variation of LL energy by external electric and magnetic fields, provides key insights into the nature of the ground state, which has been employed to probe the magnetization of quantum Hall states [30] and many-body enhanced susceptibility [31] in two-dimensional electron gas (2DEG).

In order to obtain the energetics in BLG with electric and magnetic field, we employ magnetocapacitance studies in a hexagonal boron nitride (hBN) encapsulated dual-gated BLG device. At zero magnetic field, using our quantum capacitance measurement we measure the gap around the charge neutrality point as a function of perpendicular electric field($\bar{D}$), where the obtained value of the gap matches well with the previously reported values [32]. In the presence of perpendicular magnetic field, we observe LL crossing in our magnetocapacitance measurements with $\bar{D}$. The gap closing and reopening of the lowest LL with $\bar{D}$ and $B$ shows the transition from one ordered state to another one. The values of critical electric field ($\bar{D}_c$) required to close the gap as a function of magnetic field matches well with the earlier

*anindya@iisc.ac.in

 

reports [20,27]. We further obtain the energetics of the LLs as a function of $\bar{D}$ and $B$, where the renormalization of the LL spectrum at higher electric field ($\bar{D} > 0.5$ V/nm) is clearly visible. It has been shown theoretically that at higher electric fields the LLs collapses at the band edge due to LL coupling and hybridization [1,33,34], which has not been observed experimentally prior to this report.

## II. EXPERIMENTAL DETAILS

Dual-gated bilayer graphene device was fabricated using van der Waals assembly following the procedure developed by Wang *et al.* [35]. Briefly bilayer graphene was first mechanically exfoliated onto a piranha cleaned $Si/SiO_2$ substrate from a bulk single crystal of natural graphite. On another clean substrate, hBN was mechanically exfoliated and potential thin hBN was looked at for using the optical microscope. Using dark-field microscope imaging, hBN flake with uniform smooth surface and free of bubbles was chosen. hBN, BLG, and hBN were picked up sequentially, one on top of another, and the complete stack (hBN-BLG-hBN) was deposited onto a $n++$ doped $Si/SiO_2$ substrate with 285 nm oxide. The stack was then annealed at 200 °C in vacuum to get a uniform surface free of bubbles. The electrical contacts were fabricated using electron-beam lithography followed by etching the hBN-BLG-hBN stack, and one-dimensional contact was established by thermally evaporating Cr/Au (5/70 nm) [35]. Another step of lithography and thermal deposition was carried out to define the topgate electrode [see Supplemental Material (SM) [36], Sec. I, for details]. The optical image of the final device is shown in Fig. 1(a). The schematic of the device and the measurement scheme are shown in Fig. 1(b). The top hBN thickness ∼11 nm and bottom hBN thickness ∼15 nm were measured using atomic force microscopy (see SM [36], Sec. II). The thickness of the top hBN was found independently using a period of oscillation of the capacitance minima in the magnetic field [37]. The excellent dielectric properties of hBN serve the purpose of using a thin gate dielectric for measuring a detectable change in total capacitance ($C_t$). All the measurements were carried out in a $^3$He refrigerator with a base temperature of $T \sim 240$ mK.

For the capacitance measurements we have used the measurement scheme described in our earlier works [38,39] using a home-built differential current amplifier with a gain of $10^7$. The capacitance has been measured between the top-gate electrode and BLG with a small ac excitation voltage of ∼10–15 mV at a frequency of ∼5 kHz [36,40–43] with a resolution of $\sim 0.5\, fF$. All wires were shielded to reduce the parasitic capacitance. In a parallel-plate capacitor made of a normal bulk metal and a two-dimensional material like graphene, adding a charge requires electrostatic energy, but also kinetic energy, due to the change in chemical potential, thereby contributing to the total capacitance [44]. The total measured differential capacitance in such a system is given by

$$C_t = \left(\frac{1}{C_g} + \frac{1}{C_q}\right)^{-1} + C_p, \tag{1}$$

where $C_g$ is the geometric capacitance; $C_q = Se^2\frac{dn}{d\mu}$ is the quantum capacitance; $e$ is the electronic charge; $S$ is the

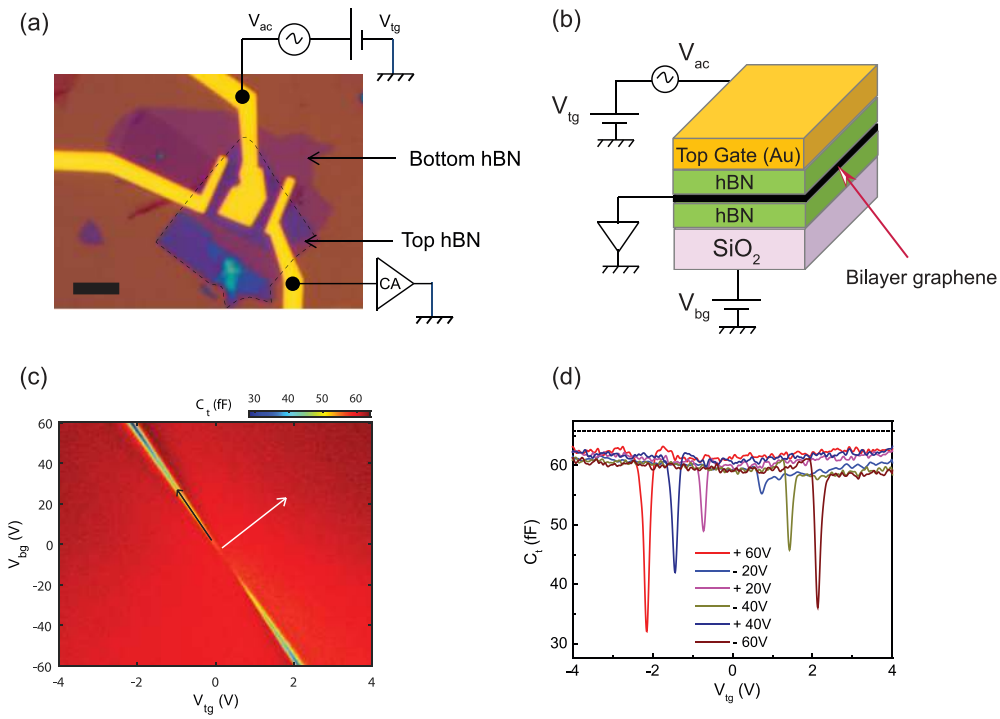


FIG. 1. (a) Optical image of the device. Scale bar 5 $\mu$m. (b) Schematic of the device architecture and measurement scheme. (c) Color plot of measured total capacitance ($C_t$) as a function of backgate voltage ($V_{bg}$) and topgate voltage ($V_{tg}$) at $T \sim 240$ mK. Black solid line shows the $\bar{D}$ axis, and white solid line shows the $n$ axis. (d) Cut lines showing $C_t$ as a function of topgate voltage $V_{tg}$ for several values of backgate voltage ($V_{bg}$).

area under the top-gate electrode; $\frac{dn}{d\mu}$ is the thermodynamic compressibility; and $C_p$ is the parasitic capacitance arising due to the wirings plus the stray capacitances. In BLG, the application of electric field between the layers results in breaking the inversion symmetry, which in turn opens up a band gap [32] at the charge neutrality point. Dual-gated geometry allows us to independently control electronic density ($n$) and electric displacement field ($\bar{D}$) under the topgated region. The net transverse electric field in a dual-gated device is given by $\bar{D} = [C_{bg}(V_{bg} - V^0_{bg}) - C_{tg}(V_{tg} - V^0_{tg})]/2\epsilon_0$, and the total carrier density is given by $n = [C_{bg}(V_{bg} - V^0_{bg}) + C_{tg}(V_{tg} - V^0_{tg})]/e$; $\epsilon_0$ is the vacuum permittivity, $e$ is the electronic charge, $C_{bg}(C_{tg})$ is the capacitance per unit area of the backgate (topgate) region, and $V^0_{bg}, V^0_{tg}$ are the charge neutrality points.

### III. CAPACITANCE DATA AT $B = 0$ T

Figure 1(c) shows the color plot of the measured total capacitance $C_t$ as a function of backgate voltage ($V_{bg}$) and topgate voltage ($V_{tg}$) at $B = 0$ T. The data was taken by sweeping the topgate voltage for different values of backgate voltages. Tuning of topgate and backgate changes both the total carrier density ($n$) and the band gap ($\Delta_g$). The diagonal white solid line marked in Fig. 1(c) shows the direction of $n$, and the solid black line shows the direction of $\bar{D}$. For $\bar{D} \sim 0$, $C_t$ exhibits a minimum at zero density, signifying the hyperbolic nature of band structure for the ungapped bilayer graphene [46]. As $|\bar{D}|$ increases, the capacitance minima decreases, revealing the formation of gap in the energy spectrum in the bilayer graphene [47]. The diagonal line in Fig. 1(c) corresponds to the charge neutrality point under the topgated region. Along the diagonal line the capacitance minima decreases, signifying the electric-field-induced band-gap opening. The charge neutrality points ($V^0_{tg}, V^0_{bg}$) are located at 0.3 and –8.5 V. From the slope of the diagonal line we can effectively estimate the ratio of the capacitive coupling between the top and bottom gates $C_{tg}/C_{bg} \sim 27$. [$C_{tg}\Delta V_{tg} = C_{bg}\Delta V_{bg}$ along the diagonal line in Fig. 1 c, $d_{bg} \sim 300$ nm, $\epsilon_{hBN} = \epsilon_{SiO_2} \sim 3.9$, yields $d_{tg} \sim 10.75$ nm, which matches well with the value of $d_{tg} \sim 11$ nm obtained using atomic force microscopy (AFM), see SM [36], Sec. II.] Figure 1(d) shows the cut lines of $C_t$ as a function of $V_{tg}$ for several values of $V_{bg}$. The geometric capacitance $C_g \sim 66\,fF$ is marked with a dashed black line. Noting the area of our device $S \sim 21\ \mu\text{m}^2$, the effective geometric capacitance was $C_g \sim 66\,fF$. The parasitic capacitance was estimated by comparing the experimental capacitance data at $\bar{D} = 0$ with the theoretical one [Eq. (1)], where the only adjusting parameter was $C_p$. (See SM [36], Sec. III; the density of states for ungapped bilayer graphene with effective mass $m_* = 0.03m_e$ was calculated from Ref. [1].) The parasitic capacitance $C_p$ in our device is ∼152 fF. This value of $C_p$ is subtracted from all the data presented in this paper.

In order to get a better insight to the experimental data, we need to extract the quantum capacitance ($C_q$) as a function of Fermi energy ($E_F$) from the experimentally measured $C_t$ as a function of backgate and topgate voltages. The Fermi energy and band gap are independently controlled by changing $V_{bg}$ and $V_{tg}$. Thus the quantum capacitance should be extracted along the constant $\bar{D}$ lines as a function of Fermi energy. We have followed a similar approach as described in Ref. [48] (see SM [36], Sec. IV, for details). The Fermi energy of bilayer graphene is given by the charge conservation relation $E_F = e\int_0^{V_{tg}}(1 - \frac{C_t}{C_g})dV_{tg}$ [49]. Figure 2(a) shows the color plot of total capacitance ($C_t$) as a function of Fermi energy and electric field. It can be seen that the band gap opens with the increment of $\bar{D}$. The maximum $\bar{D}$ we could reach was 0.8 V/nm with a band-gap opening $\Delta_g \sim 80$ meV, in agreement with previously reported values [32]. The extracted quantum capacitance ($C_q^{-1} = C_t^{-1} - C_g^{-1}$) for several values of $\bar{D}$ is shown in Fig. 2(b). It can be seen that with the increment of $\bar{D}$, $C_q$ decreases, signifying the increase of band gap. We have observed asymmetry in the $C_q$ for the electron and hole side, which has also been previously observed by other groups [47,48]. The $1/\sqrt{E}$ Van Hove singularity is also observed at the band edge as predicted [50]. The extracted $\Delta_g$ as a function of $\bar{D}$ has been shown in Fig. 2(c). The measured band-gap values match well with the theoretical band gap calculated using a tight-binding model [45].

### IV. MAGNETOCAPACITANCE DATA

The competing magnetic and electric field leads to various interesting phases in the LL spectrum of BLG. To visualize the

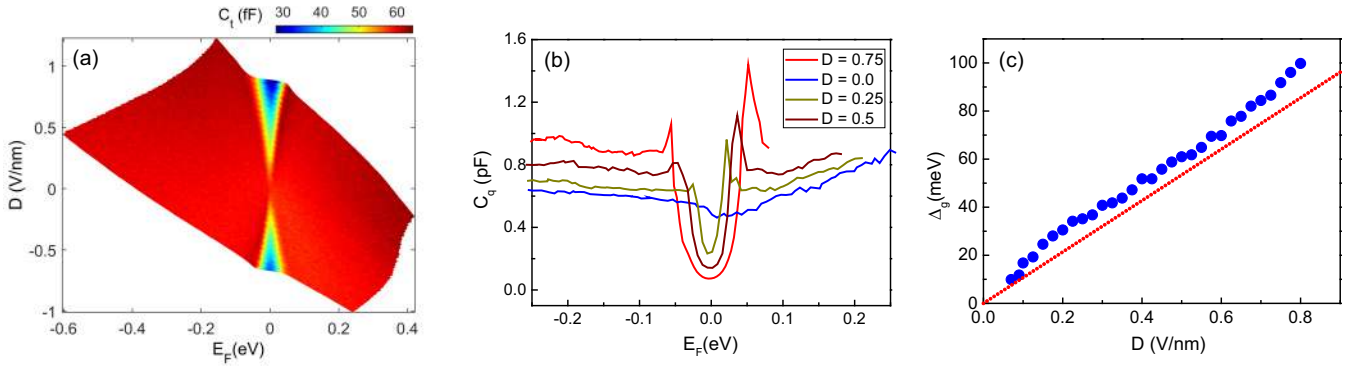


FIG. 2. (a) Color plot of total capacitance ($C_t$) as a function of electric field ($\bar{D}$) and Fermi energy $E_F$. (b) Extracted quantum capacitance ($C_q$) with $E_F$ for different value of $\bar{D}$. (c) Blue scattered plots shows the extracted band gap as a function of electric field $\bar{D}$. Red dashed line shows the calculated band gap with $\bar{D}$ (Refs. [16,45]).

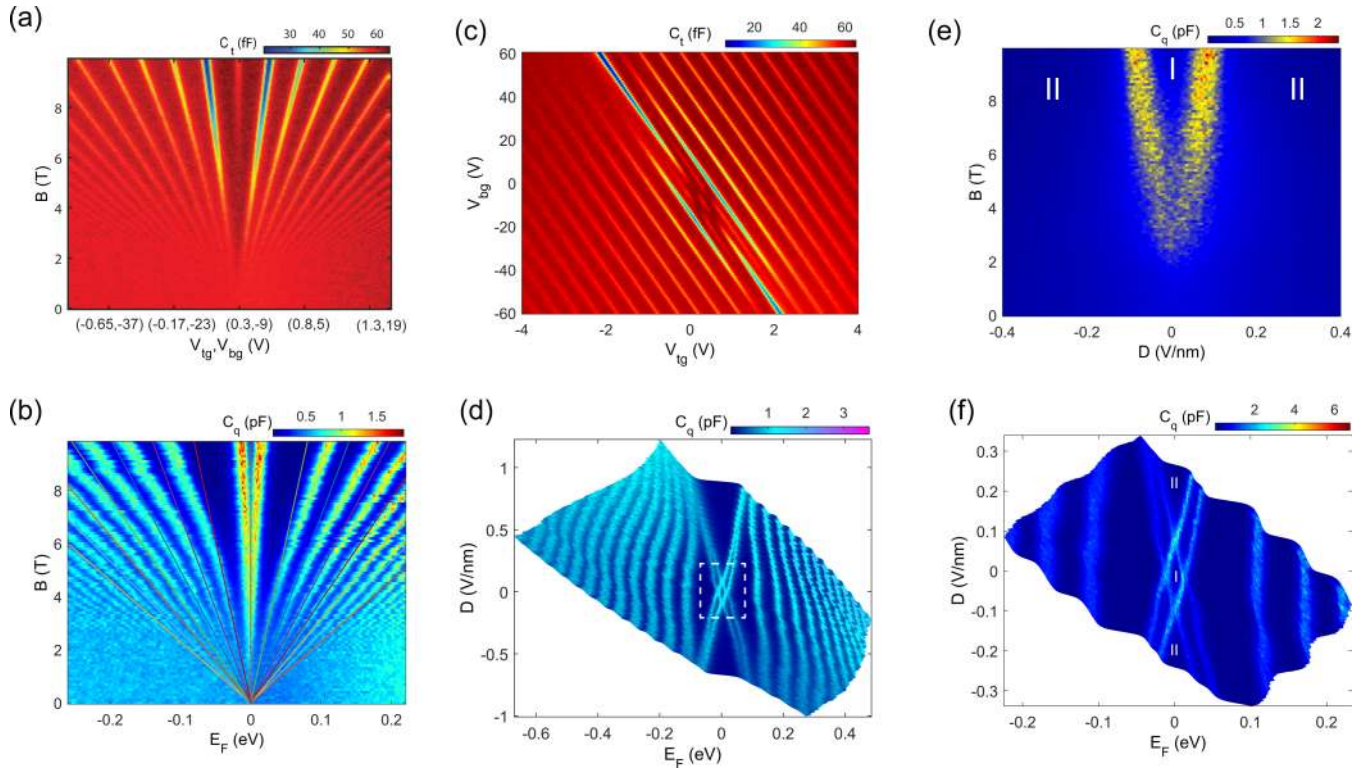


FIG. 3. (a) Color plot of the measured total capacitance ($C_t$) for $\bar{D} = 0$ as a function of magnetic field ($B$). The data was recorded synchronously by sweeping $V_{tg}$ ($V_{tg}$) keeping $\bar{D} = 0$. (b) Extracted quantum capacitance ($C_q$) as a function of $E_F$ for different values of magnetic field for $\bar{D} = 0$. The solid lines are the single-particle LL energy spectrum of BLG as discussed in the main text. (c) Color plot of the measured total capacitance ($C_t$) as a function of ($V_{tg}$, $V_{bg}$) for $B = 10$ T. (d) Extracted quantum capacitance ($C_q$) as a function of Fermi energy $E_F$ and electric field ($\bar{D}$) at $B = 10$ T. (e) Color plot of $C_q$ as a function of $\bar{D}$, and $B$ for $E_F = 0$. (f) $C_q$ as a function of $E_F$, for small value of $\bar{D}$ [zoomed-in region of Fig. 3(d) labeled in white dashed box]. Different insulating phase has been labeled by I and II.

energetics of the LLs as a function of $\bar{D}$ and $B$, we present our magnetocapacitance data. For an ungapped pristine BLG, in the absence of any interactions, the LL energies in a perpendicular magnetic field are given by $E_N = \pm\hbar\omega_c\sqrt{N(N-1)}$, where $\omega_c = eB/m^*$ is the cyclotron frequency and $N = 0, \pm1, \pm2\ldots$ are the orbital index. For $N = 0, 1$; $E_N = 0$. Thus, the zeroth-energy LL is eightfold degenerate, whereas all other Landau levels ($N \geqslant 2$) are fourfold degenerate (two spins and two valleys) [1].

Figure 3(a) shows the experimental LL fan diagram for $\bar{D} = 0$. Here, $C_t$ was measured by sweeping $V_{tg}, V_{bg}$ synchronously, keeping the $\bar{D} = 0$ and changing only the carrier density. The dips in the capacitance data correspond to the LL gap. The gap around the zeroth LL start appearing for $B > 5$ T. The LL corresponding to $N = \pm2, \pm3, \pm4$ can be seen in Fig. 3(a). The geometric capacitance $C_g$ was determined independently from the fact that spacing $\Delta V_{tg}$ between the adjacent capacitance minima in Fig. 3(a) is given by the amount of charge required to fill each Landau level [37] ($C_g \Delta V_g = \frac{4Se^2B}{h}$, where $\Delta V_g \sim 0.48$ V) (see SM [36], Sec. V), yielding an effective $C_g \sim 65.5\, fF$, which matches quite well as extracted from the color plot of Fig. 1(c) and AFM imaging (see SM [36], Sec. II). The conversion of the $x$ axis in Fig. 3(a), which is a combination of topgate voltage and backgate voltage, to Fermi energy is shown in the SM [36], Sec. VI. Figure 3(b) shows the result of such a conversion, where we plot the extracted $C_q$ as a function Fermi energy for different values of magnetic field. The solid lines are generated using single-particle LL energies for ungapped BLG ($E_N = \pm\hbar\omega_c\sqrt{N(N-1)}$, with effective mass $m_* = 0.03m_e$). It can be seen that up to $B < 6$ T, the extracted LL spectrum matches quite well with the theory. However, for $B > 6$ T we observe noticeable mismatch between the experimental and the theoretical values (10%–15%), which has also been addressed in previous studies, employing magnetocapacitance measurements [37,39,42]. This mismatch has been attributed to the inaccurate conversion in determining $E_F$ at higher magnetic field as the bulk becomes more insulating, leading to the increase in the series resistance (R) component. In the SM [36], Sec. IX, we have shown the in-phase (R) and out-of-phase (C) component at $B = 10$ T, where one can see the resistive component is an order of magnitude smaller compared to the capacitive impedance, and thus our measurements are predominately governed by the capacitance. A detailed discussion is given in the Supplemental Material [36], Sec. IX.

We now show the LL spectrum as a function of electric and magnetic field. Figure 3(c) shows the measured $C_t$ as a function of $V_{bg}$ and $V_{tg}$ for $B = 10$ T. In Fig. 3(d) we have shown the extracted quantum capacitance as a function of $E_F$ and $\bar{D}$ for $B = 10$ T. The parallel lines are the different LLs which evolve with $\bar{D}$. The most striking feature is the evolution of the zeroth-energy LL with $\bar{D}$. In Fig. 3(f) we have

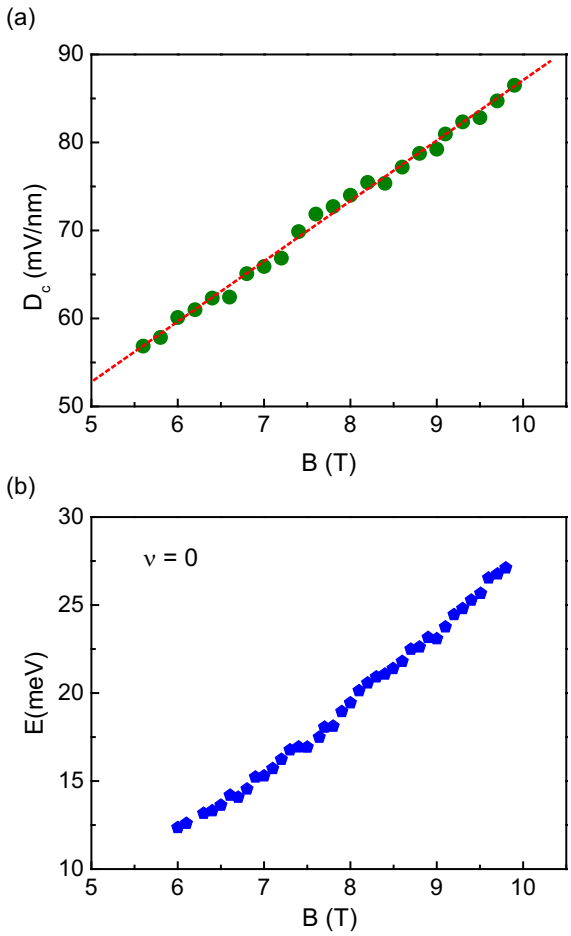


FIG. 4. (a) Critical electric field ($\bar{D}_c$) as a function of $B$. (b) The LL energies for $\nu = 0$ state as a function of $B$ for $\bar{D} = 0$.

shown the zoomed-in part of the central region of Fig. 3(d) (labeled in the white dashed box). The emergence of the $\nu = 0$ insulating state [labelled as (I) in Fig. 3(f)] can be seen for $\bar{D} = 0$. With the increment of $\bar{D}$, we see the evolution of the $\nu = 0$ insulating state. For small values of $\bar{D}$, the $\nu = 0$ state remains gapped; with an increase in $\bar{D}$, the gap decreases monotonically; and then for a critical value $\bar{D}_c = 0.08$ mV/nm, the gap closes; and with further increase in $\bar{D}$, the gap again reopens [labelled as (II)] and remains gapped for high $\bar{D}$ (maximum $\bar{D}$ for our device was $\bar{D} \sim 1$ V/nm). This electric-field-induced gap closing and reopening from region I to II is a signature of phase transition [23]. In Fig. 3(e) we show the evolution of the $\nu = 0$ state with $\bar{D}$ and $B$. Here, the topgate and backgate were swept synchronously to maintain zero carrier density and vary only $\bar{D}$ as described earlier. It can be seen that the insulating region labeled as I in Fig. 3(e) is separated out by two insulating regions labeled by II. The yellow region shows the gap closing between regions I and II. Figure 4(a) shows the plot of critical electric field ($\bar{D}_c$),where the gap closes as a function of $B$. The critical electric field ($\bar{D}_c$), which determines the transition point, can be written as a linear function of magnetic field as $\bar{D}_c = \bar{D}_{\text{off}} + \alpha B$, where $\bar{D}_{\text{off}}$ is the offset electric field and $\alpha$ is the slope. For our case, $\bar{D}_{\text{off}} = 18$ and $\alpha = 7$ mV/nm $\times B[T]$, which matches well with the theoretically predicted values [51] and experimentally observed values for $\bar{D}_c$ reported using resistance measurements [20], suggesting a spin-polarized ground state at zero $\bar{D}$ (labelled I).

Thus the $\nu = 0$ QHS undergoes a phase transition between the spin-polarized phase (labelled as region I) and the layer-polarized phase (labelled as region II) in the $(B - \bar{D})$ plane. Furthermore the $\nu = 0$ gap at $\bar{D} = 0$ as a function of magnetic field is shown in Fig. 4(b), where the gap increases linearly with $B$, with a slope of 3 meV/T, which is in agreement with previous reports [29], suggesting that the ground state is spin polarized (for $\bar{D} = 0$, labeled as region I) and rules out the possibility that the ground state is valley polarized [15].

## V. LANDAU LEVELS WITH HIGH ELECTRIC FIELD

Theoretical work employing tight-binding calculations have shown that the existence of interlayer bias between the layers ($U$) will have a compelling effect on the LL spectrum of BLG [52]. In this section we discuss the evolution of the LL spectrum with high interlayer bias. Figure 5(a) shows the LL energies as a function of $\bar{D}$ for $B = 6$ T. One striking feature is the reduction of the energy separation between the LLs as the band gap increases, especially between the LLs near the band edge. For $\bar{D} > 0.5$ V/nm we see the LLs near the band edge merge with each other. Figure 5(b) shows a color plot of the LL spectrum (as $C_q$) as a function of $E_F$ for $\bar{D} = 0.8$ V/nm ($\Delta_g \sim 80$ meV). One can clearly see the differences between the LL spectrum at $\bar{D} = 0$ [Fig. 3(b)] and $\bar{D} = 0.8$ V/nm [Fig. 5(b)]. At $\bar{D} = 0$ the LLs are clearly visible at $B = 2$ T, whereas at $\bar{D} = 0.8$ V/nm LLs can be hardly seen even at $B = 8$ T. It can be also seen from the Fig. 5(b) that the LLs are broadened and that the broadening is higher for lower LLs near the band edge. In Fig. 5(c), we also show the evolution of the gap for the $\nu = 2$ state as a function of $\bar{D}$ for B = 10 T. One can notice that for a fixed magnetic field the LL gap decreases almost linearly with increasing $\bar{D}$. It has been shown theoretically in Ref. [53] that the LL spectrum in the presence of $B$ and $\bar{D}$ has the following energy eigenvalues for $n > 0$:

$$E^{\pm}_{n,s_1,-} = \left(n + \frac{1}{2}\right)\beta\tilde{\Delta} \mp \beta U + s_1\sqrt{\left[(2n+1)\beta U \mp \frac{\beta\tilde{\Delta}}{2} - U\right]^2 + n(n+1)\,\beta^2\gamma_1^2}, \tag{2}$$

where $\gamma_1 = 0.4$ eV, $\tilde{\Delta} = 59$ meV, $\beta = \frac{\omega_0^2}{\gamma_1^2}$, $\omega_0 = \sqrt{2}\frac{\hbar v_0}{l_B}$; $l_B$ is the magnetic length, and $v_0 = \sqrt{3}\gamma_0 a_0/\hbar \approx 1.0 \times 10^8$ cm/s is the Fermi velocity. Figure 5(d) shows the calculated LL energies as a function of energy gap ($U$) for $B = 6$ T. The solid and the dashed lines correspond to $K$ and $K'$ valleys. The LLs start to merge for $U > 50$ meV, which matches well with the experimentally observed values, as can be seen in Fig. 5(a). We do not observe the splitting of the $K$ and $K'$ valleys due to

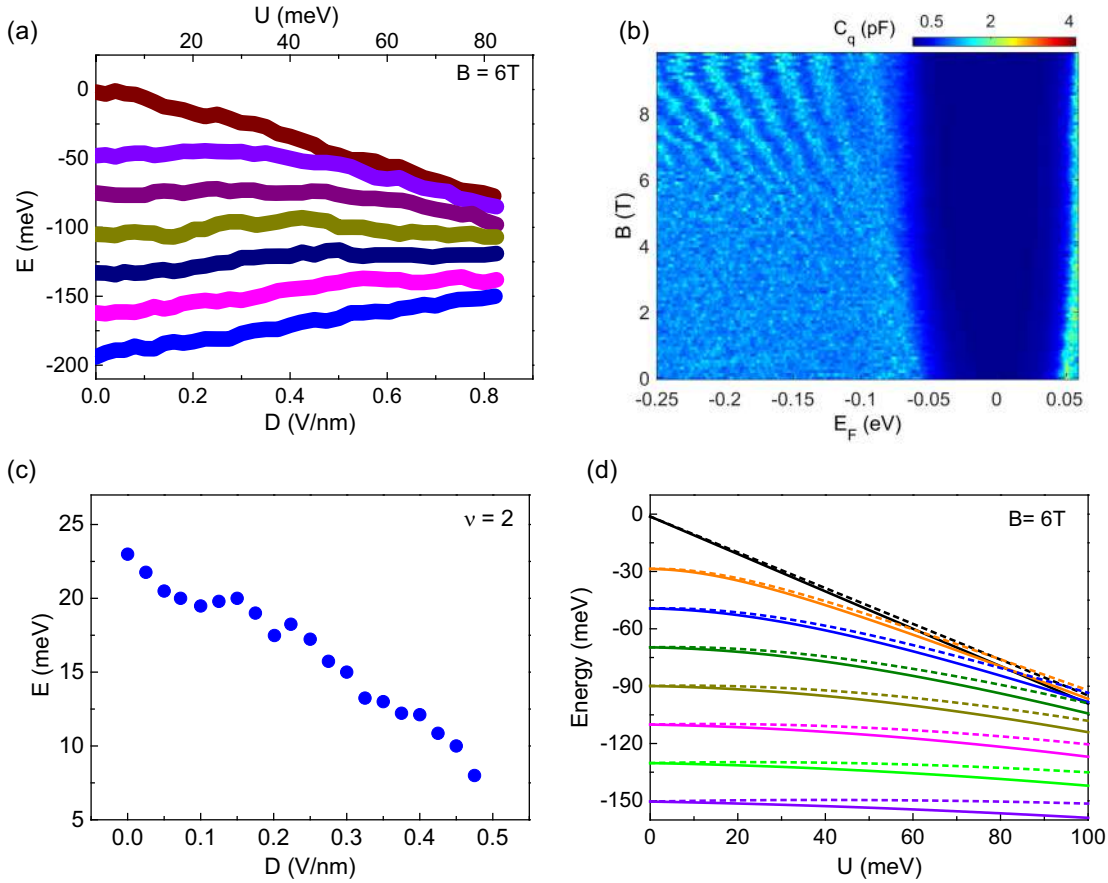


FIG. 5. (a) LL energies as a function of electric field ($\bar{D}$) for $B = 6$ T. (b) Extracted quantum capacitance ($C_q$) as a function of $E_F$ for different values of magnetic field at $\bar{D} = 0.8$ V/nm. (c) Evolution of the $\nu = 2$ gap as a function of electric field for $B = 10$ T. (d) Theoretical LL energies as a function of interlayer bias ($U$) for $B = 6$ T.

the large broadening of our device ($\delta E_F \sim 20$ meV); instead we observe the broadening of the LLs with increasing $\bar{D}$.

## VI. CONCLUSION

In summary, we have mapped the complete energetics of the Landau-level spectrum in a bilayer graphene with magnetic and electric field. We model a possible ground state based on our observations. We have also demonstrated the smearing of the LLs at high broken inversion symmetry, in agreement with theoretical predictions.

## ACKNOWLEDGMENTS

A.D. thanks Department of Science and Technology (DST), Government of India, under Grants No. DSTO1470 and No. DSTO1597 for financial support.

[1] E. McCann and V. I. Fal'ko, Phys. Rev. Lett. **96**, 086805 (2006).
[2] T. Ohta, A. Bostwick, T. Seyller, K. Horn, and E. Rotenberg, Science **313**, 951 (2006).
[3] R. Nandkishore and L. Levitov, Phys. Rev. Lett. **104**, 156803 (2010).
[4] F. Freitag, J. Trbovic, M. Weiss, and C. Schönenberger, Phys. Rev. Lett. **108**, 076602 (2012).
[5] R. Nandkishore and L. Levitov, Phys. Rev. B **82**, 115124 (2010).
[6] Y. Wang, H. Wang, J.-H. Gao, and F.-C. Zhang, Phys. Rev. B **87**, 195413 (2013).
[7] O. Vafek and K. Yang, Phys. Rev. B **81**, 041401 (2010).
[8] F. Zhang and A. H. MacDonald, Phys. Rev. Lett. **108**, 186804 (2012).
[9] B. E. Feldman, J. Martin, and A. Yacoby, Nat. Phys. **5**, 889 (2009).
[10] P. Maher, L. Wang, Y. Gao, C. Forsythe, T. Taniguchi, K. Watanabe, D. Abanin, Z. Papić, P. Cadden-Zimansky, J. Hone *et al.*, Science **345**, 61 (2014).
[11] J. Li, Y. Tupikov, K. Watanabe, T. Taniguchi, and J. Zhu, Phys. Rev. Lett. **120**, 047701 (2018).
[12] J. Velasco, Jr., Y. Lee, Z. Zhao, L. Jing, P. Kratz, M. Bockrath, and C. Lau, Nano Lett. **14**, 1324 (2014).
[13] B. Hunt, J. Li, A. Zibrov, L. Wang, T. Taniguchi, K. Watanabe, J. Hone, C. Dean, M. Zaletel, R. Ashoori *et al.*, Nat. Commun. **8**, 948 (2017).
[14] P. Maher, C. R. Dean, A. F. Young, T. Taniguchi, K. Watanabe, K. L. Shepard, J. Hone, and P. Kim, Nat. Phys. **9**, 154 (2013).

[15] A. Kou, B. E. Feldman, A. J. Levin, B. I. Halperin, K. Watanabe, T. Taniguchi, and A. Yacoby, Science **345**, 55 (2014).

[16] K. Lee, B. Fallahazad, J. Xue, D. C. Dillen, K. Kim, T. Taniguchi, K. Watanabe, and E. Tutuc, Science **345**, 58 (2014).

[17] F. Freitag, M. Weiss, R. Maurand, J. Trbovic, and C. Schönenberger, Phys. Rev. B **87**, 161402 (2013).

[18] J. Velasco, Jr., L. Jing, W. Bao, Y. Lee, P. Kratz, V. Aji, M. Bockrath, C. Lau, C. Varma, R. Stillwell *et al.*, Nat. Nanotechnol. **7**, 156 (2012).

[19] H. J. van Elferen, A. Veligura, E. V. Kurganova, U. Zeitler, J. C. Maan, N. Tombros, I. J. Vera-Marun, and B. J. van Wees, Phys. Rev. B **85**, 115408 (2012).

[20] S. Kim, K. Lee, and E. Tutuc, Phys. Rev. Lett. **107**, 016803 (2011).

[21] J. Velasco, Jr., Y. Lee, F. Zhang, K. Myhro, D. Tran, M. Deo, D. Smirnov, A. MacDonald, and C. Lau, Nat. Commun. **5**, 4550 (2014).

[22] E. V. Gorbar, V. P. Gusynin, V. A. Miransky, and I. A. Shovkovy, Phys. Rev. B **85**, 235460 (2012).

[23] B. J. LeRoy and M. Yankowitz, Science **345**, 31 (2014).

[24] M. Kharitonov, Phys. Rev. B **86**, 075450 (2012).

[25] M. Kharitonov, Phys. Rev. Lett. **109**, 046803 (2012).

[26] M. Kharitonov, Phys. Rev. B **86**, 195435 (2012).

[27] R. T. Weitz, M. T. Allen, B. E. Feldman, J. Martin, and A. Yacoby, Science **330**, 812 (2010).

[28] A. Zibrov, C. Kometter, H. Zhou, E. Spanton, T. Taniguchi, K. Watanabe, M. Zaletel, and A. Young, Nature (London) **549**, 360 (2017).

[29] J. Martin, B. E. Feldman, R. T. Weitz, M. T. Allen, and A. Yacoby, Phys. Rev. Lett. **105**, 256806 (2010).

[30] E. De Poortere, E. Tutuc, S. Papadakis, and M. Shayegan, Science **290**, 1546 (2000).

[31] J. Zhu, H. L. Stormer, L. N. Pfeiffer, K. W. Baldwin, and K. W. West, Phys. Rev. Lett. **90**, 056805 (2003).

[32] Y. Zhang, T.-T. Tang, C. Girit, Z. Hao, M. C. Martin, A. Zettl, M. F. Crommie, Y. R. Shen, and F. Wang, Nature (London) **459**, 820 (2009).

[33] F. Guinea, A. H. Castro Neto, and N. M. R. Peres, Phys. Rev. B **73**, 245426 (2006).

[34] Y.-H. Ho, S.-J. Tsai, M.-F. Lin, and W.-P. Su, Phys. Rev. B **87**, 075417 (2013).

[35] L. Wang, I. Meric, P. Huang, Q. Gao, Y. Gao, H. Tran, T. Taniguchi, K. Watanabe, L. Campos, D. Muller *et al.*, Science **342**, 614 (2013).

[36] See Supplemental Material at http://link.aps.org/supplemental/10.1103/PhysRevB.99.125411 for details about device fabrication, parasitic capacitance estimation, conversion of gate voltage to Fermi energy, and effect of frequency. The Supplemental Material contains Refs. [35,37,40–43,48].

[37] G. Yu, R. Jalil, B. Belle, A. S. Mayorov, P. Blake, F. Schedin, S. V. Morozov, L. A. Ponomarenko, F. Chiappini, S. Wiedmann *et al.*, Proc. Natl. Acad. Sci. USA **110**, 3282 (2013).

[38] M. Kuiri, C. Kumar, B. Chakraborty, S. N. Gupta, M. H. Naik, M. Jain, A. Sood, and A. Das, Nanotechnology **26**, 485704 (2015).

[39] M. Kuiri, G. K. Gupta, Y. Ronen, T. Das, and A. Das, Phys. Rev. B **98**, 035418 (2018).

[40] R. K. Goodall, R. J. Higgins, and J. P. Harrang, Phys. Rev. B **31**, 6597 (1985).

[41] T. P. Smith, B. B. Goldberg, P. J. Stiles, and M. Heiblum, Phys. Rev. B **32**, 2696 (1985).

[42] G. Yu, R. Gorbachev, J. Tu, A. Kretinin, Y. Cao, R. Jalil, F. Withers, L. Ponomarenko, B. Piot, M. Potemski *et al.*, Nat. Phys. **10**, 525 (2014).

[43] F. Chiappini, S. Wiedmann, K. Novoselov, A. Mishchenko, A. K. Geim, J. C. Maan, and U. Zeitler, Phys. Rev. B **92**, 201412 (2015).

[44] S. Luryi, Appl. Phys. Lett. **52**, 501 (1988).

[45] H. Min, B. Sahu, S. K. Banerjee, and A. H. MacDonald, Phys. Rev. B **75**, 155115 (2007).

[46] E. A. Henriksen and J. P. Eisenstein, Phys. Rev. B **82**, 041412 (2010).

[47] A. F. Young, C. R. Dean, I. Meric, S. Sorgenfrei, H. Ren, K. Watanabe, T. Taniguchi, J. Hone, K. L. Shepard, and P. Kim, Phys. Rev. B **85**, 235458 (2012).

[48] K. Kanayama and K. Nagashio, Sci. Rep. **5**, 15789 (2015).

[49] S. Dröscher, P. Roulleau, F. Molitor, P. Studerus, C. Stampfer, K. Ensslin, and T. Ihn, Appl. Phys. Lett. **96**, 152104 (2010).

[50] E. McCann and M. Koshino, Rep.Prog. Phys. **76**, 056503 (2013).

[51] C. Tőke and V. I. Fal'ko, Phys. Rev. B **83**, 115455 (2011).

[52] J. M. Pereira, F. M. Peeters, and P. Vasilopoulos, Phys. Rev. B **76**, 115419 (2007).

[53] L. M. Zhang, M. M. Fogler, and D. P. Arovas, Phys. Rev. B **84**, 075451 (2011).